Journal of Colloid and Interface Science 683 (2025) 1077–1086

Contents lists available at ScienceDirect

Journal of Colloid And Interface Science

journal homepage: www.elsevier.com/locate/jcis

Regular Article

Probing the Self-Assembly dynamics of cellulose nanocrystals by X-ray photon correlation spectroscopy

Jiajun Tian [a], Ahmad Reza Motezakker [b,c], Ruifu Wang [a], Andrew J. Bae [a], Andrei Fluerasu [d], Hengwei Zhu [a], Benjamin S. Hsiao [a,*], Tomas Rosén [c,e,*]

[a] Department of Chemistry, Stony Brook University, Stony Brook, NY 11794-3400, United States
[b] Department of Mechanics, KTH Royal Institute of Technology, SE-100 44 Stockholm, Sweden
[c] Wallenberg Wood Science Center, KTH Royal Institute of Technology, SE-100 44 Stockholm, Sweden
[d] National Synchrotron Light Source II, Brookhaven National Laboratory, Upton, NY 11973-5000, United States
[e] Department of Fibre and Polymer Technology, KTH Royal Institute of Technology, SE-100 44 Stockholm, Sweden

GRAPHICAL ABSTRACT

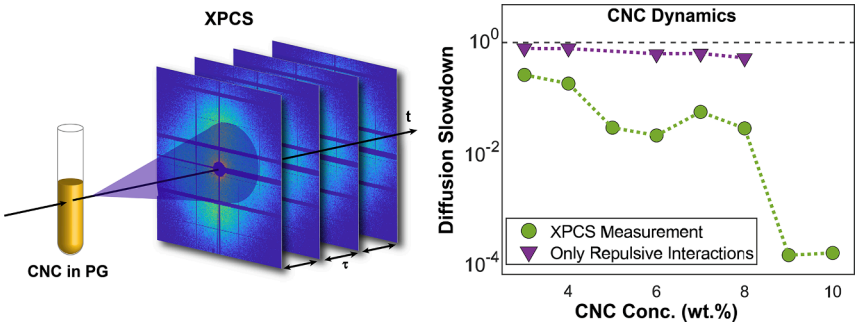

ARTICLE INFO

Keywords:
X-ray Photon Correlation Spectroscopy
Cellulose Nanocrystals
Self-Assembly
Dynamics
Phase Transition

ABSTRACT

Hypothesis: Charge-stabilized colloidal cellulose nanocrystals (CNCs) can self-assemble into higher-ordered chiral nematic structures by varying the volume fraction. The assembly process exhibits distinct dynamics during the isotropic to liquid crystal phase transition, which can be elucidated using X-ray photon correlation spectroscopy (XPCS).

Experiments:: Anionic CNCs were dispersed in propylene glycol (PG) and water spanning a range of volume fractions, encompassing several phase transitions. Coupled with traditional characterization techniques, XPCS was conducted to monitor the dynamic evolution of the different phases. Additionally, simulated XPCS results were obtained using colloidal rods and compared with the experimental data, offering additional insights into the dynamic behavior of the system.

Findings:: The results indicate that the particle dynamics of CNCs undergo a stepped decay in three stages during the self-assembly process in PG, coinciding with the observed phases. The phase transitions are associated with a total drop of Brownian diffusion rates by four orders of magnitude, a decrease of more than a thousand times slower than expected in an ideal system of repulsive Brownian rods. Given the similarity in the phase behaviors in CNCs dispersed in PG and in water, we hypothesize that these dynamic behaviors can be extrapolated to other

* Corresponding authors.
E-mail addresses: benjamin.hsiao@stonybrook.edu (B.S. Hsiao), trosen@kth.se (T. Rosén).

https://doi.org/10.1016/j.jcis.2024.12.234
Received 12 February 2024; Received in revised form 29 October 2024; Accepted 29 December 2024
Available online 31 December 2024

polar solvent environments. Importantly, these findings represent the direct measurement of CNC dynamics using XPCS, underscoring the feasibility of directly assessing the dynamic behavior of other rod-like colloidal suspensions.

1. Introduction

Self-assembly of rod-like molecules/particles is observed across different anisotropic colloidal systems. From the organization of lipid molecules into bilayer structures in cell membranes of living organisms to the formation of periodic structures in photonic crystal displays, the distinct structure can form unique properties in materials for various research fields [1–3]. In this context, understanding the temporal evolution of colloidal systems through dynamic characterizations provides essential insights into the structural evolution mechanisms and assembly pathways of these anisotropic building blocks. For example, the dynamic information, such as particle interactions and particle diffusion, can offer the assessment of structural stability for colloidal systems. Such an understanding of the dynamic behavior has significant implications for the design and fabrication of colloidal assemblies [4,5].

Among self-assembly colloidal systems, cellulose nanocrystals (CNCs) represent as a class environmentally friendly and sustainable natural-based anisotropic nanomaterial for many emerging applications. CNCs possess a rod-like shape with chirality along the cellulose chains. Their high surface charge enables good dispersion in water, where the dispersed CNC particles can self-assemble into a chiral nematic liquid crystal (LC) phase at high concentrations [6–8]. The unique properties of self-assembled CNCs can be used in remediation and biomedical materials, optics, photonics, sensing, antimicrobial coatings, and drug delivery systems [9–13]. The self-assembly behavior of CNC exhibits a series of phase transitions from isotropic to arrested phases, representing a complex process. The average structures such as the particle dimensions, interparticle distances and structure sizes of the self-assembled states have been characterized previously by various characterization techniques, including polarized optical microscopy (POM) [14–21], scanning electron microscopy (SEM) [22,23,24], and small-angle X-ray scattering (SAXS) [17,25,26]. While understanding the mechanism of the CNC self-assembly process, tracking particle dynamics during the aggregation of CNC colloids can offer more direct insights than merely the characterization of static structures. The self-assembled structures are known to be less Brownian-like, thus can be manipulated through external fields, such as hydrodynamic forcing to control the alignment of CNCs. Previously, dynamic light scattering (DLS) has been employed to study the dynamics of CNCs in dilute and semi-dilute concentration states [26–28]. For example, Uhlig *et al.* studied the CNC aggregation at different concentrations by DLS [27]. By assuming a spherical shape for the CNC aggregates, they calculated the hydrodynamic diameters of the colloidal suspension, using these values as a means to estimate the average size of the CNC aggregates. Moreover, the dynamic dimensions of individual CNC in dilute suspensions were extracted from the translational and rotational diffusion coefficients in DLS measurements. Boluk *et al.* integrated Broersma's relationship with these two diffusion coefficients to determine the particle dimensions, including both mean diameter and length of CNC [28]. However, the CNC suspensions at relatively high concentrations (above 5 wt%) are difficult to measure by DLS due to the issue of multiple scattering [29]. This limitation can be overcome by using coherent X-rays as the light source, where its theoretical basis for the data analysis is the same as that for DLS [30–32]. As a result, X-ray photon correlation spectroscopy (XPCS) can complement DLS to investigate the dynamics of CNCs across different phases at a broad range of concentration.

For this purpose, the present study demonstrates the use of XPCS, complemented by DLS, to investigate the dynamics of self-assembled structures of CNCs from the isotropic phase, liquid crystal (LC) phase to a kinetically arrested state. To slow down the dynamics in the suspension state for measurement, propylene glycol (PG) was chosen as a primary dispersion medium. Based on our findings, we hypothesize that the observed dynamics of CNCs in PG can extend to other polar solvents including water, owing to the similarity in the phase behavior of CNC colloids in the suspension state. Typically, the dynamic behavior of CNCs in the aqueous suspension at high concentrations is too fast to be observed by XPCS.

2. Experimental Section

2.1. Materials

CNC suspensions prepared from never-dried wood pulp using the hydrolysis approach (using sulfuric acid) were provided by the Process Development Center of the University of Maine, USA. The obtained CNC had a sulfur content of 1.1 wt%, where its aqueous suspension (CNC-H_2O) possessed a mass fraction of 10.3 wt%. The CNC particle dimensions were measured in a previous study by Rosén *et al.* giving the lengths between 150 and 300 nm and widths between 10 and 30 nm (by transmission electron microscopy, TEM) [33]. Propylene glycol (PG) was purchased from VWR International (Pennsylvania, USA).

The CNC-PG suspensions were prepared by a solvent exchange method reported in previous studies [34,35]. In brief, CNC aqueous suspensions were premixed with PG of different masses to achieve a desired mass fraction of CNC in PG at concentrations between 3 and 10 wt%. Subsequently, water was removed under reduced pressure at 50 °C using the rotary evaporation approach. Supplementary rheological characterization of the CNC suspensions in water and PG at different concentrations are listed in the *Supporting Information*.

2.2. Polarized optical microscopy (POM)

The POM images of CNC suspensions were obtained using an Olympus BX51 Epifluorescent and Polarized Imaging Microscope (Olympus Life Science, Massachusetts, USA) at Center for Functional Nanomaterials (CFN), Brookhaven National Laboratory (BNL), USA. The suspension was sealed into a parallel glass cell for observation. As the sample birefringence increased with the CNC concentration, the light passed through the cross polarizer would increase. To obtain clear images in the POM setup, the background light was turned dimmer with the increase in CNC concentration.

2.3. Dynamic light scattering (DLS)

The apparent diffusion coefficient of CNC-PG and CNC-H_2O at low concentrations was characterized by DLS. The upper bound of CNC concentration for an accurate determination of dynamics in water (CNC-H_2O) and PG (CNC-PG) was found to be around 5 wt% and 6 wt%, respectively (see Section 6 in *Supporting Information*). DLS measurements were conducted on a Brookhaven Instruments Nanobrook Omni Particle Sizer (Brookhaven Instruments, New York, USA) equipped with a 40 mW red diode laser (nominal wavelength of 640 nm) at an angle of 90°. The measured scattering vector q for CNC-PG and CNC-H_2O suspensions were $0.00145 Å^{-1}$ *and* $0.00185 Å^{-1}$. DLS experiments were conducted at 25 °C, and each sample was measured at least three times using a 4 mL plastic cuvette to obtain the average and standard deviation. Particle size distributions were determined using a non-negative least squares (NNLS) analysis. Peaks emerging at a lower size range (< 10 nm) were taken as artifacts and excluded from the analysis.

2.4. X-ray photon correlation spectroscopy (XPCS)

Simultaneous XPCS and SAXS measurements of CNC-PG suspensions were conducted at the Coherent Hard X-ray Scattering (CHX) beamline, National Synchrotron Light Source II (NSLS-II), BNL, USA. These XPCS/SAXS measurements employed synchrotron X-ray with a wavelength of 1.28 Å. In the measurement, CNC-PG suspensions were injected into 1 mm quartz capillary tubes and then placed on the holder with a sample-to-detector distance of 16.0 m. The scattered X-rays were collected by the Eiger detector (Eiger X 4 M, Dectris, 75 × 75 μm^2 pixel size). Each XPCS measurement included 4000 frames with a maximum data acquisition time of 1.34 ms at 750 Hz. The data was assessed at q from 0.00237 to 0.00663 Å^{-1}, where $q = \frac{4\pi}{\lambda}\sin\left(\frac{\theta}{2}\right)$ with θ being the scattering angle to the incident X-ray.

In the XPCS study, a coherent X-ray beam was focused on the sample. A sequence of detector images was then recorded to capture the time-dependent scattering intensity $I(q,t)$ emerging from the interference of the coherent X-ray and the sample. The temporal fluctuations of the scattering intensity (i.e., the *speckle* pattern) were analyzed by the intensity-intensity autocorrelation function:

$$g^{(2)}(q,\tau) = \frac{\langle I(q,t)I(q,t+\tau)\rangle}{\langle I(q,t)\rangle^2} \quad (1)$$

The autocorrelation $g^{(2)}(q,\tau)$ was calculated from the azimuthal average of all the scattering intensities at a certain q at a delay time τ. To avoid radiation damage, the data was collected and stitched together from three specific beam attenuation levels and exposure times (Fig. S1 in *Supporting Information*), and the results are shown in Table 1. For each setup, a total of 2500 images were recorded, spanning delay times in the range $\tau = 10^{-4}$ to 10 s without having a full dose equivalent higher than 0.60 s. For reference, this is a less than 10 times smaller dose than was previously observed to influence the dynamics in the system of nanocellulose in PG [36].

To analyze the autocorrelation function, $g^{(2)}$ was further normalized into $C(\tau) = (g^{(1)})^2$ via the Siegert relation:

$$g^{(2)}(\tau) = 1 + \beta(g^{(1)}(\tau))^2 \quad (2)$$

where $g^{(1)}$ is the first-order autocorrelation function and β is the scattering contrast obtained by calibration using a static membrane. In an ideal system of monodisperse spherical nanoparticles with radius R, the square first-order autocorrelation becomes $C(\tau) = \exp(-2Dq^2\tau)$, with diffusion coefficient $D = k_BT/(6\pi\eta R)$, and k_B and T being the Boltzmann constant and temperature, respectively. In the dense CNC systems, the dynamics as measured through XPCS can be more difficult to assess. Normalized correlation functions $C(\tau)$ of CNC-PG of concentration 3–10 wt% at two repeating XPCS measurements are shown in Figs. S2 and S3, and the resulting effective diffusion coefficient (D_{eff}) values fitted by the KWW model are shown in Fig. S4, *Supporting Information*.

2.5. Coarse-Grained molecular dynamic (MD) simulations

The coarse-grained MD simulations were performed using the ESPResSo (Extensible Simulation Package for Research on Soft Matter) software [37]. The system was simulated in a cubic box with sides of 500 nm with periodic boundary conditions. Each individual CNC was represented with a string of 15 spherical beads having a diameter 10 nm. The system was then freely evolving due to Brownian motion according to a PG viscosity of $\eta = 0.042$ *Pa·s* and temperature of $T = 300K$. A weight percentage was calculated based on a cellulose density of 1.5 $\frac{g}{cm^3}$. The repulsive interaction between CNCs was simulated using a Weeks-Chandler-Andersen potential [38]. The simulation was initially validated by comparing theoretical expressions for Brownian motion of rod-like particles. The reciprocal space as observed by a detector in the simulated XPCS experiment was obtained through a Fourier transform using the positions of individual beads, the same way as in earlier work [36]. The autocorrelation data was obtained and analyzed in the same way as in the experiment in a q range of 0.004 – 0.014 Å^{-1}. The details about the simulations are described in Section 2 of *Supporting Information*.

Table 1
X-ray intensity attenuation and exposure time setups that were stitched together.

	Attenuated intensity (%)	Exposure time, t_{exp} (ms)	Total dose, equivalent of full dose (s)
1	96.4	9.994	0.600
2	81	1.334	0.625
3	0	0.114	0.275

3. Results and Discussion

3.1. Phase behavior of CNC colloids in PG by POM

Generally, the phase behavior of how the structure of anionic CNC colloids varies with concentration is illustrated in Fig. 1a, with expected dynamics summarized in Table 2. This figure illustrates that at low concentrations (Regime 0), particles are oriented randomly in an isotropic phase with weak particle interactions, moving relatively freely due to Brownian motion. With increasing concentration, the rod-like nanoparticles interact, and it becomes entropically favorable to self-assemble into locally aggregated ellipsoidal LC structures, called *tactoids* (Regime I). In this phase, tactoids are freely moving and are isotopically distributed, but Brownian motion is slowed down due to the collective motion of CNCs [33]. With more CNCs in the system, tactoids grow and coalesce into larger LC domains. When the concentration increases and reaches a critical value C_1, bigger tactoids can be influenced by gravity and form cholesteric LC layers [15,21,24,39], with expected slower dynamics. The concentration range where the isotropic tactoids coexist with these cholesteric layers is denoted as a biphasic state (Regime IIa). When another critical CNC concentration C_2 is reached, no isotropic tactoids remain, and the entire system becomes liquid crystalline (Regime IIb), but there is still some mobility for CNCs to rearrange into long-range ordered structures in the system. Finally, when past another critical concentration C_3, the system becomes an arrested glass (Regime III), where CNCs are 'caged' by the interactions of local particles thus there is no mobility to rearrange. The structure remains kinetically stationed in the initial state set by deformation during the sample preparation [7,16]. The system has a nematic ordering in this state, but there is no mobility to rearrange into a chiral form.

In this study, CNC-PG colloids follow the expected phase behavior, and the emergence of LC structures can be easily observed with POM through the transmitted light intensity (the sample is sandwiched between two linear cross-polarizers to reveal the material birefringence). The POM images of CNC-PG suspensions with different concentrations are shown in Fig. 1b. As the isotropic phase exhibits no birefringence, it remains dark under POM. At 3 wt%, isolated tactoids were visible, indicative of a transition to Regime I. As the system enters the biphasic region, the LC layering dominates the texture in the POM image, which is visible through the periodic fringes of brighter and darker intensities. The transition to this regime, Regime II, occurs around 5 wt%. At 9 wt%, the LC fringes disappear under optical microscope in the CNC-PG system as the system enters the arrested glassy state of Regime III [40].

3.2. Dynamics characterization by XPCS

The diffusive dynamics of the CNC-PG colloids at the different concentrations were studied with XPCS. The experimental setup of the XPCS measurement is illustrated in Fig. 2a. The q dependence of the

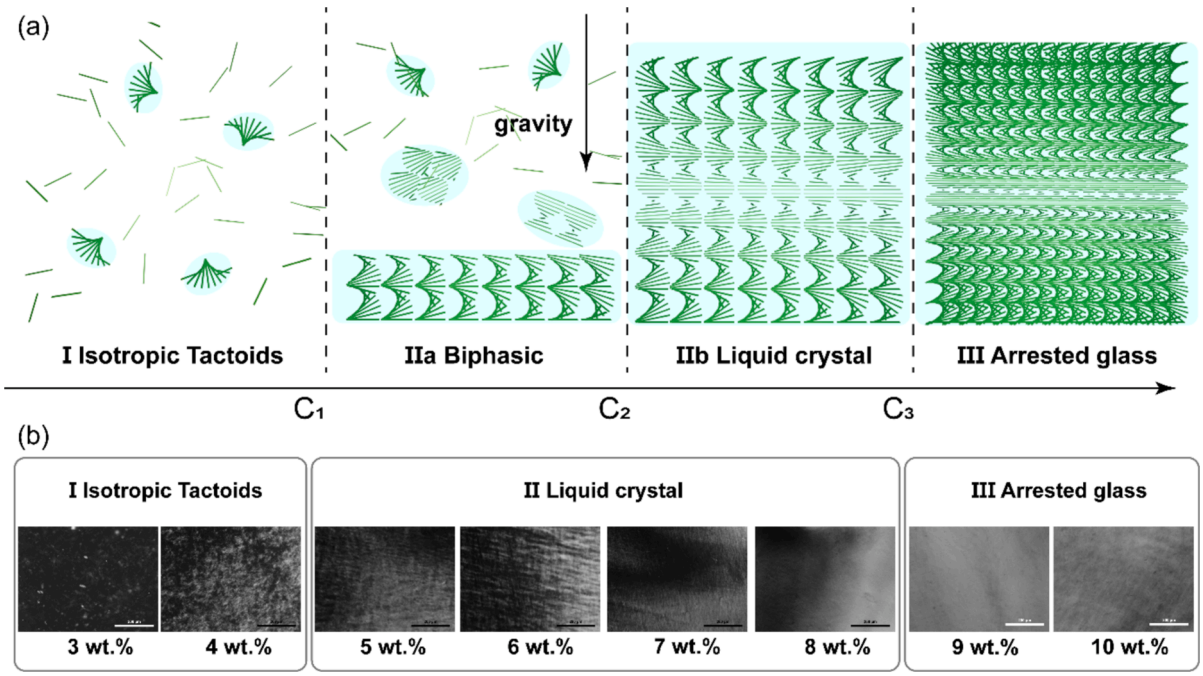

Fig. 1. (a) Schematic illustrations and (b) POM images of CNCs dispersed in PG at various concentrations with a visual identification of the phase regimes described in Table 2. The scale bars in each POM image correspond to 200 μm.

Table 2
Phase behavior and expected dynamics of CNC suspensions at increasing concentrations. The mixed dynamics include both Brownian motions from isotropic, tactoids and liquid crystalline phases.

Regime	Phase	Order	Expected dynamics
0	Isotropic	No ordering	Fast
I	Isotropic tactoids	Local	Moderate
IIa	Biphasic	Local & cholesteric	Mixed dynamics
IIb	Liquid crystalline	Cholesteric	Slow
III	Arrested glass	Nematic	Extremely Slow

experimental XPCS data was firstly analyzed to assess the possibility of anomalous diffusion, where the relaxation rate would scale as $\Gamma \propto q^{\alpha}$ with $\alpha > 2$ for subdiffusive dynamics and $\alpha < 2$ for superdiffusive dynamics [36]. The experimental XPCS results showed that there was no obvious deviation from regular Brownian motion of $\alpha = 2$, and the overall shape of the correlation curves remained the same in the range of q studied (see Section 2 in *Supporting Information*). The dynamics of rod-like colloidal particles typically exhibit the behavior of *de Gennes* narrowing, where the dynamics can scale with the reciprocals of the structure factors [41–44]. However, compared to the increasing structure factor value in the same q range, no such behavior was observed. Moreover, considering the relatively high noise level observed in the correlation function due to the relatively low scattering power of CNCs, there is too much uncertainty for deeper interpretations of the dynamic behavior. Therefore, we focus primarily on the average dynamic behavior assuming $\Gamma \propto q^2$ with all the data for a single sample (all three detectors, two separate measurements, and all q regions) being combined into one data set and scaling delay times as $\tau^* = \tau\left(\frac{q}{q_0}\right)^2$, with $q_0 = 0.0024 \text{Å}^{-1}$ being the lowest q studied here.

Fig. 2b illustrates the square first-order autocorrelation function $C(\tau^*)$ for three different concentrations (additional concentrations are shown in Figs. S2, S3 and S5 in *Supporting Information*). Here, it is seen a clear slowdown of the dynamics when the CNC concentration is increased from 3 to 10 wt%. The decay of $C(\tau^*)$ for the intermediate concentration of 6 wt% is clearly stretched, indicative of polydisperse dynamics. To quantify the data, three different methodologies can be applied (more details in Fig. S6 and Section 3 in *Supporting Information*):

(1) Fitting $C(\tau^*)$ to a stretched exponential or the Kohlrausch–Williams–Watts (KWW) function:

$$C(\tau^*) = \exp(-2(\Gamma\tau^*)^{\gamma}). \quad (3)$$

The stretching of the correlation curve can be described by a KWW exponent of $\gamma < 1$.

(2) Assuming polydisperse Brownian dynamics, we a regularized inverse Laplace transformation of $C(\tau^*)$ can be applied using the CONTIN algorithm [45] by assuming a sum of exponential modes:

$$C(\tau^*) = \sum_i G_i \exp(-2\Gamma_i\tau^*). \quad (4)$$

The mean relaxation rate Γ can be obtained through a weighted average of the decay modes. The stretching of the correlation curve can be described by the width of the relaxation rate distribution G_i, which can be quantified with a polydispersity index *PDI* through a cumulant expansion.

$C(\tau^*)$(3) can be fitted with a simple exponential function:

$$C(\tau^*) = \exp(-2\Gamma\tau^*), \quad (5)$$

which does not take the stretched shape into account but provides a good estimation of the mean relaxation rate.

All three methods were used to determine an apparent diffusion coefficient using $D_{app} = \Gamma/q_0^2$. An example of the three methodologies applied to the XPCS data of CNCs in PG at 6 wt% is shown in Fig. 2c. Here, both the stretched exponential function and the polydisperse Brownian model provide good fits to the combined data. These two functions mainly differ in the limit of small values of τ^*. As there is very little additional information from the experimental data, the correct functional form cannot be conclusively determined here. We note that the simple exponential fit will naturally not match the data perfectly in cases where $C(\tau^*)$ is stretched, but it was found to yield a good estimation of the mean relaxation rate.

From the above analysis, we assess the apparent diffusion coefficient

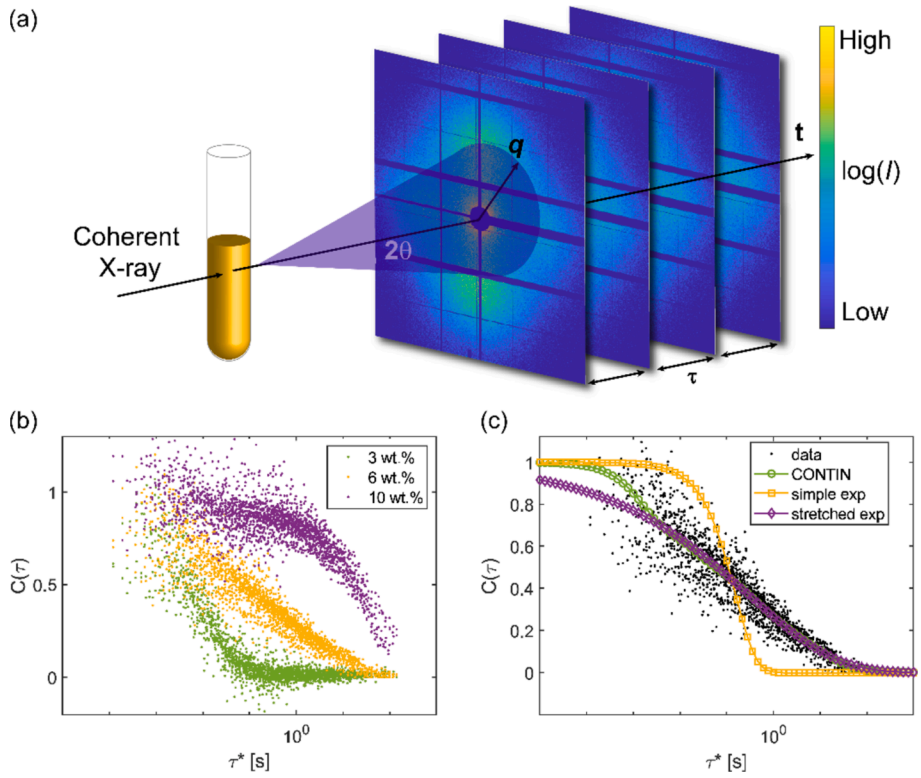

Fig. 2. Schematic illustration of the XPCS experiment and example results from the XPCS experiments of CNC-PG suspensions and subsequent analysis: (a) XPCS experimental setup, (b) the square first-order autocorrelation data $C(\tau^*)$ of suspensions at varying CNC concentrations, (c) the $C(\tau^*)$ data at 6 wt% analyzed with three different methodologies.

D_{app} derived from the DLS measurement at low CNC concentrations using the same CONTIN procedure. Typically, the DLS measurements can be used to reveal the particles size distributions of CNC-H_2O and CNC-PG (Figs. S7 and S8, *Supporting Information*). Using the CONTIN method, the normalized apparent diffusion coefficient ratio (D_{app}/D_o) was calculated from the DLS data for both CNC-PG and CNC-H_2O suspensions (Figs. S9-S12, *Supporting Information*). We note that the D_{app} was normalized by D_o, which should be the diffusion coefficient of an ideal dilute system (Regime 0 in Table 2). The D_{app}/D_o values for CNC-PG and CNC-H_2O determined by DLS at the CNC concentrations from 0.5 – 4 wt% are illustrated in Figs. S13 and S14, respectively.

At higher concentrations (> 4 wt%), the CNC dynamics in PG can only be assessed by the XPCS study. The fitting of correlation function C (τ) and distribution of the relaxation rate G(Γ) from the CONTIN analysis of the XPCS data from CNC-PG suspensions at high concentrations are shown in Figs. S15 and S16. From the analysis, the D_{app}/D_o value as a function of CNC concentration is shown in Fig. 3a ($D_o = 4.23 \times 10^{-13} m^2/s$ determined from 0.5 wt% of CNC in PG in the dilute isotropic phase was used as the referenced value). We notice that the D_{app}/D_o values of CNC-PG obtained from DLS (Fig. S13, *Supporting Information*) and XPCS (Fig. 3a) at CNC concentrations of 3 wt% and 4 wt % are very similar to each other indicating the complementary nature of these two techniques. Fig. 3b illustrates the γ and *PDI* values as a function of CNC concentration in PG. It is seen that regardless of the analytical methodology chosen, the values of D_{app}/D_0 exhibit a similar trend as function of the CNC concentration. It is also observed that the D_{app} value is the lowest for the stretched KWW function, which can be attributed to the non-comparable nature of the mean relaxation rate obtained from this function, when compared to a sum of the exponential decays [46]. The trend of D_{app}/D_0 clearly consists of two distinct

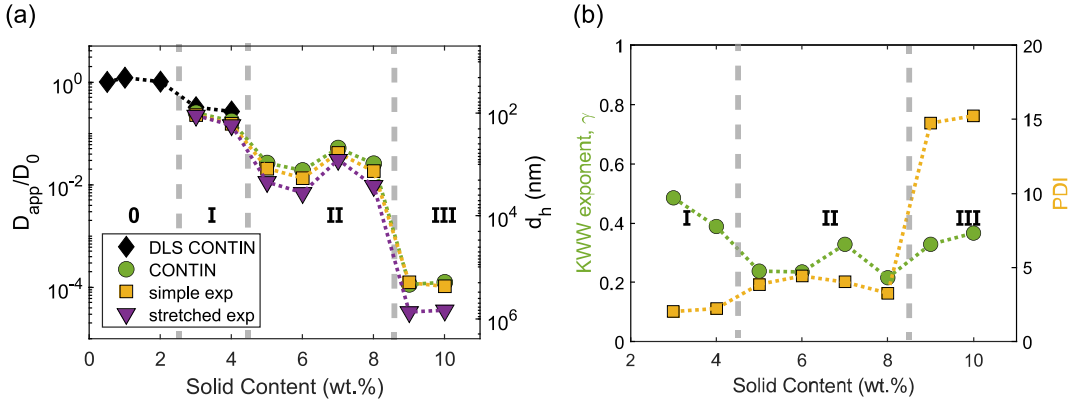

Fig. 3. The results from the analysis of XPCS data for CNC-PG suspensions: (a) apparent diffusion coefficients D_{app} normalized by the diffusion coefficient of a dilute system D_0 and the corresponding hydrodynamic diameter d_h, (b) the KWW exponent γ and PDI from the CONTIN analysis.

transitions in dynamic behavior, coinciding with the expected phase transitions to the biphasic state (Regime I to Regime II) and the arrested glass state (Regime II to Regime III).

In Fig. 3, several unique features can be observed. With the CNC concentration increases from 2 to 3 wt%, the transition from Regime 0 to Regime I appeared to be associated with the notable dynamics slowdown, as indicated by the decrease in D_{app}/D_o. The corresponding hydrodynamic diameters d_h, calculated via the Stokes-Einstein equation, can be used to represent the effective sizes of CNC tactoids [47]. Thus, the mean apparent size of tactoids in Regime I should be around 100 nm, corresponding to the mean length of individual CNCs.

Since the data values obtained by XPCS from 3 and 4 wt% CNC-PG suspensions are consistent with the DLS results, the dynamic slowdown due to the formation of CNC tactoids captured by XPCS is validated. Thus, the XPCS results at higher CNC concentrations (5 to 8 wt%) can reveal the dynamic behavior of CNCs in a liquid crystal dominating state, Regime II. In this regime, the D_{app}/D_o values appear to remain quite stable in the order of 10^{-2}. The sudden decrease in D_{app} from the Regimes I and II transition reflects the formation of a chiral nematic phase. This phase imposes higher order and anisotropy in the structure, thus dramatically reducing the freedom of the particle movement. In other words, the formation of stacked layered liquid crystal structures limited the rotational diffusion of the rod-like CNCs, resulting in a sudden drop in the overall diffusion coefficient. Furthermore, the system contains a broader range of dynamic time scales, as indicated with a lower KWW exponent γ and higher polydispersity index *PDI*. The likely reason for this observation is that the system is undergoing constant thermal reconfigurations (rotation and translation) with a variety of sizes of collective structures in a slow process towards a phase-separated equilibrium. The occasional higher value of D_{app}/D_0 is likely due to the inhomogeneity caused by the difference in sample loading, and the possibility of small air bubbles in the system.

Finally, as CNCs in PG transition into an arrested glass state in Regime III (9 to 10 wt%), there is a dramatic slowdown of the dynamics with two orders of magnitude reduction in D_{app}/D_0 (the value is in the order of 10^{-4}) from 8 to 9 wt%. Assuming a mean-square displacement of L^2 for major reconfigurations, this would take around 10 ms in the dilute system, but around a minute in the arrested state. The significant slowdown in the CNC dynamics can be attributed to the formation of the arrested glass structure. In this state, CNCs have strong inter-particle interactions and even entanglements, which further reduces the freedom of particle movement. Additionally, there is a dramatic increase in the apparent polydispersity *PDI* during this regime. Interestingly, it is seen that there may be a two-stage decay at higher concentration (9 and 10 wt%), i.e., a faster dynamic mode accompanying the slow dynamics as shown in Fig. S5 in *Supporting Information.* This observation has been observed before and attributed to the caging motion and the relaxation of structural network, respectively [48]. In other words, when the system is slowly reconfiguring in the arrested glass, stresses can be built up and released with the stress-release dynamics occurring on a much faster time scale.

3.3. *Understanding XPCS Timescales in rod-like systems using Coarse-Grained molecular dynamics (MD) simulations*

To put the above experimental results into perspective and to

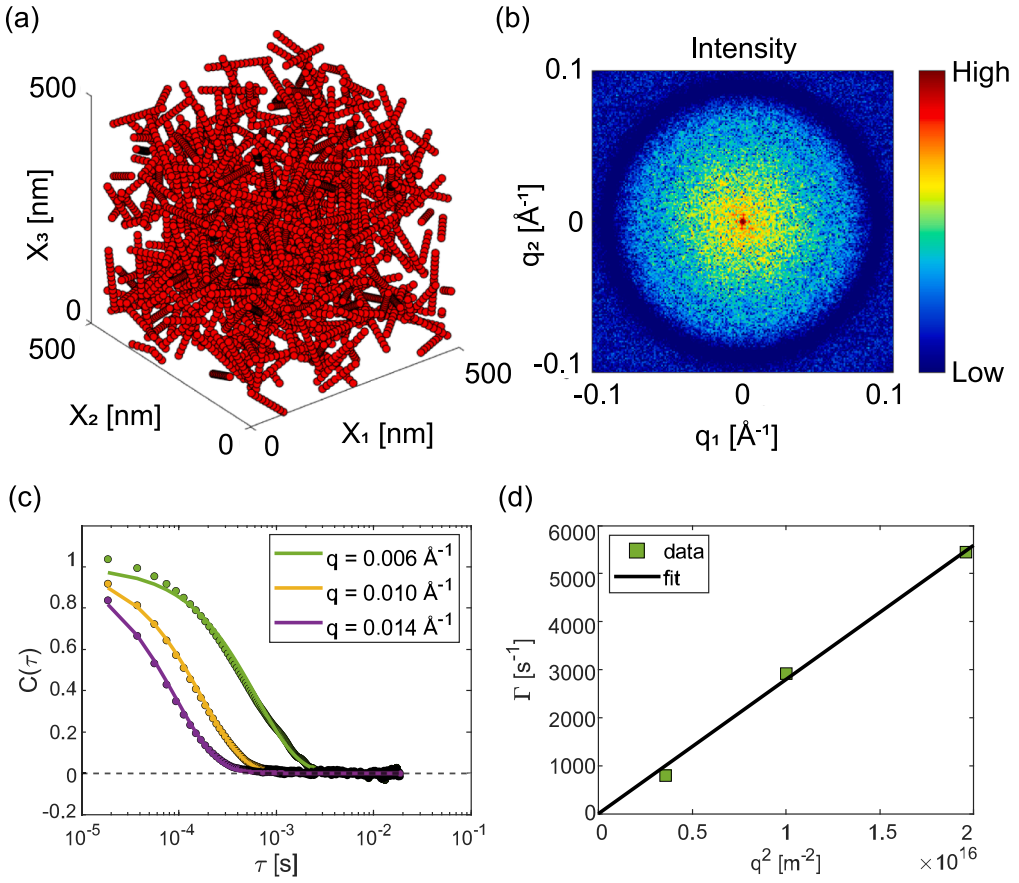

Fig. 4. Illustration of the coarse-grained MD simulations and simulated XPCS: (a) a simulated CNC system at 4 wt%, (b) simulated speckle intensities on the detector, (c) autocorrelation $g^{(2)}(q,\tau)$ (symbols) along with exponential fits (curves), (d) relaxation rate Γ from fit as function of q^2(symbols); the solid line shows best fit of $\Gamma = Dq^2$ to find the diffusion coefficient D.

understand how to interpret the autocorrelation data of the denser assemblies of rod-like particles, we performed coarse-grained molecular dynamics (MD) simulations of stiff Brownian rods with similar dimensions as CNCs, based on earlier work on dilute CNC dynamics [33]. In such simulations, each particle consists of 15 connected spherical beads of size 10 nm, and thus has a total length of 150 nm. The CNCs were studied at concentrations from 0.5 to 8 wt% with simple repulsive interactions in a cubic box with periodic boundary conditions (see Fig. 4a and a Supplementary Movie). Using simulated CNCs, the sequence of speckle patterns was simulated through a Fourier transform [36], and was used to obtain autocorrelation curves in the same way as in the experiment (see Fig. 4b-4d). More details about the simulations are provided in the Materials and Methods section and Section 4 of *Supporting Information*.

In this study, the systems without any particle interactions were first simulated to validate the model using existing theoretical expressions for dilute Brownian motion of rod-like particles, where the results are illustrated in Table 3. From this analysis, we find that the simulated rotary and translational diffusion coefficients are close to the analytical values. The discrepancy for D_r can be attributed to the fact that the theory relies on spheroidal particles, which is different than the bead-model in the simulations, and that $D_r \propto L^{-3}$, which is very sensitive to particle length (see Section 4 of *SI* for further assessment). It is interesting to note that the diffusion coefficient D from simulated XPCS-experiments is significantly higher than D_t, which is due to the rotational diffusion of the particles. Comparing with D_t for individual beads making up the single CNC, we find that these two coefficients match. Consequently, we can conclude that *the measured diffusion coefficient from XPCS is based on the translational diffusion of mass elements of the particles*, which has contributions from both translation and rotation of CNCs. This value of $D_{t,bead}$ from the simulations of non-interacting CNCs will further be used as the reference value D_o for the simulated data. Since the experimental XPCS results is reflecting $D_{t,bead}$, we use this particle-based coefficient to describe what happens in the crowded system.

With the addition of repulsive interactions, we find how the diffusion coefficients can be affected by the increasingly crowded environment at higher CNC concentrations, where the results are shown in Fig. 5a. Up to the concentration of 1 wt%, both translational and rotational diffusion can be well described by the theory for the dilute system. However, above 1 wt%, there is a clear slowing down of the CNC dynamics due to the hinderance from neighboring particles. To understand such crowding effects, the crowding number based on the volume fraction Φ and aspect ratio (length/width) r_p can be calculated using the following expression [49]:

$$N = \frac{2}{3}\Phi r_p^2. \tag{4}$$

The number N represents how many CNCs can be found in a volume of a sphere with the same diameter as the CNC length. Given the aspect ratio $r_p = 15$ and density of cellulose ($1.5\,\frac{g}{cm^3}$), the weight percentage can be directly viewed as crowding number, where the critical concentration of 1 wt% corresponds to a crowding number of exactly $N = 1$. At the highest simulated concentration, where $N = 8$ (at 8 wt%), the dynamics have slowed down by approximately a factor 2.

Comparing these findings with the experimental results, we observe the significant influence of the collective arrangement of liquid crystal structures on the CNC dynamics as illustrated in Fig. 5b. In both simulated and experimental systems, there is a visible slow-down of dynamics above the concentration of 2–3 wt%. In the simulated system, this decrease of the diffusion coefficient is due to crowding of individual CNCs, but at 4 wt% it is only around 0.8 D_0. For the experimental system, with collective arrangements in tactoids, the diffusion coefficient is almost 10 times slower than that of the dilute system. As the real system of CNCs enter both the liquid crystalline and arrested states, the slow-down is even more dramatic, amounting to 1000 times slower than the expected value merely from repulsive crowding.

Since it is not easy to separate rotary diffusion from the translational diffusion using XPCS, it is difficult to study the nature of the CNC rearrangements in detail. However, in a recent related study, Wang *et al.* [47] studied the rotary diffusion of a similar suspension of CNCs in PG at 3.6 wt% after initially being hydrodynamically sheared. The slow-down of rotary diffusion was measured to be 100 times slower than that in the dilute case. Based on the present results that the overall dynamics only being slowed down 10 times, it can be concluded that the rotational diffusion is more affected than the translational diffusion in the phase containing isotropic tactoids.

It is apparent that the coarse-grained MD simulations did not capture the dynamics of the CNC self-assemblies during increasing concentration. Specifically, the model could not capture the evolution of the mean diffusion coefficient. At the highest simulated concentration (8 wt%), we find that dynamics start showing a slightly sub-diffusive trend due to crowding (see Fig. S17, *Supporting Information*). However, the model clearly did not capture the strongly polydisperse/stretched exponential decays of the experimental data. The model is still an improvement of typical effective sphere-models often used to describe diffusive dynamics [49]. Furthermore, we believe that the approach of comparing real XPCS results with numerical XPCS simulations can inspire the development of new interaction models for CNC assemblies that will be useful to validate the interpretation of experimental results.

3.4. Comparison to CNCs dispersed in water

Given that CNC colloids in polar solvents, such as water, exhibit similar phase transitions due to concentration-dependent effects, the dynamic behavior observed in CNC-PG provides insights into the dynamics of CNC colloids in other solvents. Here, we utilize water, the most common polar solvent, as a paradigmatic example to elucidate this dynamic trend. To highlight the analogous phase behavior between the two systems, we analyze the structural evolution of CNC-PG and CNC-H_2O using polarized optical microscopy (POM) and small-angle X-ray scattering (SAXS). The comparison of POM images of CNCs dispersed in water and PG at various concentrations is shown in Fig. S18 (*Supporting Information*), and that of SAXS results for the two CNC dispersion system are shown in Figs. S19 and Fig. S20. Both POM and SAXS measurements reveal that CNC-H_2O undergoes a phase transition similar to CNC-PG, with a distinct isotropic to LC transition observed at approximately 4 wt% concentration. Moreover, the interparticle distances (d-spacing) in both CNC-H_2O and CNC-PG systems determined by SAXS (Fig. S21, *Supporting Information*) exhibits a clear turning point at 4 wt%, indicating of the critical concentration for the isotropic to LC phase transition. Furthermore, the rheological behavior of both systems aligns with their respective phase transitions (see Section 10, Figs. S22 and S23, *Supporting Information*). For example, in CNC-H_2O, the ratio between the steady shear viscosity at low shear rate η_o normalized by the solvent

Table 3
Results from the coarse-grained MD simulations of non-interacting (dilute) CNCs and the corresponding results of the diffusion coefficient measured in a simulated XPCS-experiment; the value of $D_{t,bead}$ is used as the reference D_0 for the experiments.

$D_t[m^2/s]$theory	$D_t[m^2/s]$simulated	$D_r[rad^2/s]$theory	$D_r[m^2/s]$simulated	$D[m^2/s]$from XPCS-simulations	$D_{t,bead}[m^2/s]$simulated, based on beads
$1.89{\cdot}10^{-13}$	$1.82{\cdot}10^{-13}$	81.0	99.2	$2.77{\cdot}10^{-13}$	$2.79{\cdot}10^{-13}$

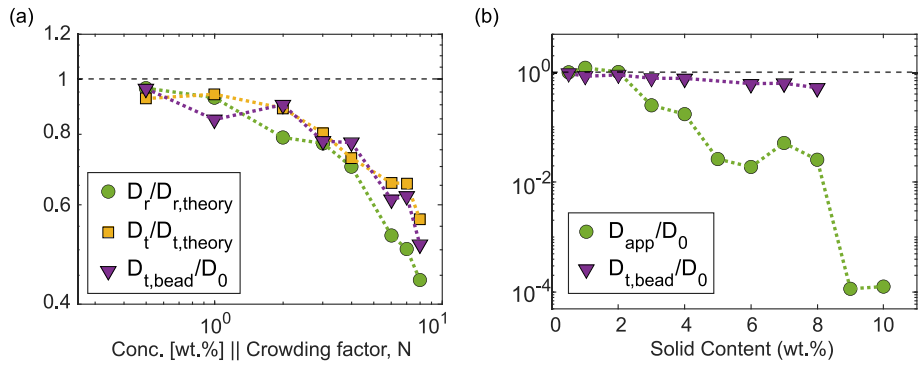

Fig. 5. Results from coarse-grained MD simulations. (a) Simulated diffusion coefficients as function of CNC concentration. (b) The simulated CNC dynamics with repulsive interactions compared with the combined normalized diffusion coefficients from DLS and XPCS measurements. The 0.5–2 wt% data is from DLS CONTIN results and the 3–10 wt% data is from XPCS CONTIN results.

viscosity η_s exhibits a stage-like slope change, where the critical concentration of 4 wt% can be determined (Fig. S22b), which is consistent with the POM and SAXS results. The consistency in the phase behavior across both systems suggests that CNC-H_2O would exhibit analogous dynamic behavior throughout the concentration rage as those in CNC-PG. Based on the dynamics results obtained from XPCS experiments of CNC-PG, we hypothesize the dynamics of CNC-H_2O suspensions containing the tactoid phase and the condensed LC phase in Fig. S24 (*Supporting Information*) that may be validated by future XPCS techniques with higher temporal resolution and brighter synchrotron X-rays. For example, future research based on new generation synchrotron source or free electron laser technology, allowing for measurements of dynamics on shorter time scales [50–52] could enable direct measurement of the dynamics of nanocellulose colloids in low viscosity solvent systems.

4. Conclusions

Based on previous studies that measured the diffusive behavior of CNC suspensions in dilute and semi-dilute regions (< 6 wt%) [26–28], this work reports direct measurements of condensed CNC dynamics (up to 10 wt%) in PG using XPCS. By combining XPCS with DLS, CNC dynamics were investigated across a broad concentration range, covering the isotropic phase, liquid crystal phase, and arrested glass state. In addition to previously reported features along CNC phase transitions, such as d-spacing [29] and viscosity [53], this work is the first to identify three distinct dynamic regimes corresponding to the (I) isotropic tactoids, (II) biphasic/liquid crystalline state, and (III) arrested glass state using XPCS. The experimentally observed dynamics were also compared with an idealized system of repulsive colloidal rods using coarse-grained molecular dynamics simulations combined with XPCS simulations. While the ideal system experiences an expected slowdown of a factor 2–4 owing to crowding effects at 10 wt%, the experimental results indicate the system slowdown exhibits a factor of 10,000, which can be attributed to the collective ordering and electrostatic interactions in the system. Given the consistent phase behavior observed in CNC colloidal systems across various polar solvents, we hypothesize that the dynamics could be extrapolated to systems exhibiting similar phase behaviors. As an example, the dynamic behaviors of CNC dispersed in water at high concentrations (not assessable by current experimental techniques) were proposed. This study underscores the potential of employing XPCS for investigating nanoscale dynamics in concentrated colloidal LC systems. The dynamics in the condensed systems such as the liquid crystal phases and the kinetic arrest states are particularly relevant to the design and manufacturing of self-assembly materials.

CRediT authorship contribution statement

Jiajun Tian: Writing – original draft, Methodology, Investigation, Formal analysis, Data curation, Conceptualization. **Ahmad Reza Motezakker:** Software, Methodology, Investigation, Formal analysis, Data curation. **Ruifu Wang:** Software, Methodology, Investigation. **Andrew J. Bae:** Software, Methodology, Investigation, Formal analysis. **Andrei Fluerasu:** Software, Methodology, Investigation, Formal analysis, Data curation. **Hengwei Zhu:** Writing – review & editing, Methodology, Investigation, Formal analysis. **Benjamin S. Hsiao:** Writing – review & editing, Supervision, Funding acquisition, Conceptualization. **Tomas Rosén:** Writing – review & editing, Writing – original draft, Supervision, Software, Project administration, Formal analysis, Conceptualization.

Declaration of competing interest

The authors declare that they have no known competing financial interests or personal relationships that could have appeared to influence the work reported in this paper.

Acknowledgement

The authors acknowledge financial support from the National Science Foundation (DMR-2216585), the Alf de Ruvo Foundation (SCA), the Hans Werthén Foundation (IVA) and Wallenberg Wood Science Center (WWSC). The authors also acknowledge experimental assistance by H. He, C. Zhan, L. Wiegart, X. Chen, S. Chodankar, and Y. Zhang as well as helpful discussions with J. Wang, D. S. Söderberg, H. Goel and O. Tschoubar. The experiments were performed at the CHX beamline (11-ID) and the LIX beamline (16-ID) of the National Synchrotron Light Source II, a U.S. Department of Energy (DOE) Office of Science User Facility operated for the DOE Office of Science by Brookhaven National Laboratory under Contract No. DE-SC0012704. The Center for BioMolecular Structure (CBMS) is primarily supported by the National Institutes of Health, National Institute of General Medical Sciences (NIGMS) through a Center Core P30 Grant (P30GM133893), and by the DOE Office of Biological and Environmental Research (KP1607011). This research used resources for rheometry and polarized microscopy of the Center for Functional Nanomaterials (CFN), which is a U.S. Department of Energy Office of Science User Facility, at Brookhaven National Laboratory under Contract No. DE-SC0012704.

Appendix A. Supplementary data

Supplementary data to this article can be found online at https://doi.org/10.1016/j.jcis.2024.12.234.

Data availability

Data will be made available on request.

References

[1] Ghosh, S.; Ray, A.; Pramanik, N. Self-assembly of surfactants: An overview on general aspects of amphiphiles. *Biophys Chem* **2020**, *265*. DOI: ARTN 106429. 10.1016/j.bpc.2020.106429.

[2] Z.W. Li, Q.S. Fan, Y.D. Yin, Colloidal Self-Assembly Approaches to Smart Nanostructured Materials, *Chem Rev* 122 (5) (2022) 4976–5067, https://doi.org/10.1021/acs.chemrev.1c00482.

[3] Y. Hu, Y.Q. Zhang, D.P. Yang, D.K. Ma, S.M. Huang, Self-assembly of colloidal particles into amorphous photonic crystals, *Mater Adv* 2 (20) (2021) 6499–6518, https://doi.org/10.1039/d1ma00477h.

[4] Y.X. Huang, C.J. Wu, J.Y. Chen, J.Y. Tang, Colloidal Self-Assembly: From Passive to Active Systems, *Angew Chem Int Edit* 63 (9) (2024), https://doi.org/10.1002/anie.202313885.

[5] I.L. Molnar, E. Pensini, M.A. Asad, C.A. Mitchell, L.C. Nitsche, L.J. Pyrak-Nolte, G. L. Miñ o, M.M. Krol, Colloid Transport in Porous Media: A Review of Classical Mechanisms and Emerging Topics, *Transport Porous Med* 130 (1) (2019) 129–156, https://doi.org/10.1007/s11242-019-01270-6.

[6] T. Benselfelt, N. Kummer, M. Nordenström, A.B. Fall, G. Nyström, L. Wågberg, The Colloidal Properties of Nanocellulose, *ChemSusChem* 16 (2023) 8, https://doi.org/10.1002/cssc.202201955.

[7] P. Lv, X. Lu, L. Wang, W. Feng, Nanocellulose-Based Functional Materials: From Chiral Photonics to Soft Actuator and Energy Storage, *Adv. Funct. Mater.* 31 (45) (2021) 2104991, https://doi.org/10.1002/adfm.202104991 (acccessed 2023-06-11T20:20:28).

[8] R.M. Parker, G. Guidetti, C.A. Williams, T. Zhao, A. Narkevicius, S. Vignolini, B. Frka-Petesic, The Self-Assembly of Cellulose Nanocrystals: Hierarchical Design of Visual Appearance, *Adv. Mater.* 30 (19) (2018) 1704477, https://doi.org/10.1002/adma.201704477 (acccessed 2023-06-06T23:54:57).

[9] Li, Y. X.; Zhang, J. J.; Zhan, C. B.; Kong, F. G.; Li, W. L.; Yang, C. F.; Hsiao, B. S. Facile synthesis of TiO2/CNC nanocomposites for enhanced Cr(VI) photoreduction: Synergistic roles of cellulose nanocrystals. *Carbohyd Polym* **2020**, *233*. DOI: ARTN 115838. 10.1016/j.carbpol.2020.115838.

[10] M. Yusefi, M.-L.-K. Soon, S.-Y. Teow, E.I. Monchouguy, B.N.H.M. Neerooa, Z. Izadiyan, H. Jahangirian, R. Rafiee-Moghaddam, T.J. Webster, K. Shameli, Fabrication of cellulose nanocrystals as potential anticancer drug delivery systems for colorectal cancer treatment, *Int. J. Biol. Macromol.* 199 (2022) 372–385, https://doi.org/10.1016/j.ijbiomac.2021.12.189.

[11] Siqueira, G.; Kokkinis, D.; Libanori, R.; Hausmann, M. K.; Gladman, A. S.; Neels, A.; Tingaut, P.; Zimmermann, T.; Lewis, J. A.; Studart, A. R. Cellulose Nanocrystal Inks for 3D Printing of Textured Cellular Architectures. *Advanced Functional Materials* **2017**, *27* (12). DOI: ARTN 1604619. 10.1002/adfm.201604619.

[12] D.A. Osorio, B.E.J. Lee, J.M. Kwiecien, X.Y. Wang, I. Shahid, A.L. Hurley, E. D. Cranston, K. Grandfield, Cross-linked cellulose nanocrystal aerogels as viable bone tissue scaffolds, *Acta Biomater* 87 (2019) 152–165, https://doi.org/10.1016/j.actbio.2019.01.049.

[13] Maturavongsadit, P.; Paravyan, G.; Shrivastava, R.; Benhabbour, S. R. Thermo-/pH-responsive chitosan-cellulose nanocrystals based hydrogel with tunable mechanical properties for tissue regeneration applications. *Materialia* **2020**, *12*. DOI: ARTN 100681. 10.1016/j.mtla.2020.100681.

[14] R. Kádár, S. Spirk, T. Nypelö, Cellulose Nanocrystal Liquid Crystal Phases: Progress and Challenges in Characterization Using Rheology Coupled to Optics, Scattering, and Spectroscopy, *ACS Nano* 15 (5) (2021) 7931–7945, https://doi.org/10.1021/acsnano.0c09829 (acccessed 2023-10-06T13:45:17).

[15] A. Tran, W.Y. Hamad, M.J. Maclachlan, Tactoid Annealing Improves Order in Self-Assembled Cellulose Nanocrystal Films with Chiral Nematic Structures, *Langmuir* 34 (2) (2018) 646–652, https://doi.org/10.1021/acs.langmuir.7b03920 (acccessed 2023-09-05T03:07:52).

[16] G. Chu, G. Vasilyev, D. Qu, S. Deng, L. Bai, O.J. Rojas, E. Zussman, Structural Arrest and Phase Transition in Glassy Nanocellulose Colloids, *Langmuir* 36 (4) (2020) 979–985, https://doi.org/10.1021/acs.langmuir.9b03570 (acccessed 2023-09-10T20:47:30).

[17] C. Schütz, M. Agthe, A.B. Fall, K. Gordeyeva, V. Guccini, M. Salajková, T.S. Plivelic, J.P.F. Lagerwall, G. Salazar-Alvarez, L. Bergström, Rod Packing in Chiral Nematic Cellulose Nanocrystal Dispersions Studied by Small-Angle X-ray Scattering and Laser Diffraction, *Langmuir* 31 (23) (2015) 6507–6513, https://doi.org/10.1021/acs.langmuir.5b00924 (acccessed 2023-06-02T03:23:05).

[18] S. Wojno, M. Fazilati, T. Nypelö, G. Westman, R. Kádár, Phase transitions of cellulose nanocrystal suspensions from nonlinear oscillatory shear, *Cellul.* 29 (7) (2022) 3655–3673, https://doi.org/10.1007/s10570-022-04474-0 (acccessed 2023-10-04T03:05:43).

[19] X. Mu, D.G. Gray, Formation of Chiral Nematic Films from Cellulose Nanocrystal Suspensions Is a Two-Stage Process, *Langmuir* 30 (31) (2014) 9256–9260, https://doi.org/10.1021/la501741r (acccessed 2023-06-07T00:02:19).

[20] J.R. Bruckner, A. Kuhnhold, C. Honorato-Rios, T. Schilling, J.P.F. Lagerwall, Enhancing Self-Assembly in Cellulose Nanocrystal Suspensions Using High-Permittivity Solvents, *Langmuir* 32 (38) (2016) 9854–9862, https://doi.org/10.1021/acs.langmuir.6b02647 (acccessed 2023-09-19T21:26:47).

[21] K.W. Klockars, B.L. Tardy, M. Borghei, A. Tripathi, L.G. Greca, O.J. Rojas, Effect of Anisotropy of Cellulose Nanocrystal Suspensions on Stratification, Domain Structure Formation, and Structural Colors, *Biomacromolecules* 19 (7) (2018) 2931–2943, https://doi.org/10.1021/acs.biomac.8b00497 (acccessed 2023-09-05T03:09:36).

[22] A. Abbasi Moud, Chiral Liquid Crystalline Properties of Cellulose Nanocrystals: Fundamentals and Applications, *ACS Omega* 7 (35) (2022) 30673–30699, https://doi.org/10.1021/acsomega.2c03311 (acccessed 2023-09-06T00:12:24).

[23] Wilts, B. D.; Dumanli, A. G.; Middleton, R.; Vukusic, P.; Vignolini, S. Invited Article: Chiral optics of helicoidal cellulose nanocrystal films. *Apl Photonics* **2017**, *2* (4). DOI: Artn 040801. 10.1063/1.4978387.

[24] P.-X. Wang, W.Y. Hamad, M.J. Maclachlan, Structure and transformation of tactoids in cellulose nanocrystal suspensions, *Nat. Commun.* 7 (1) (2016) 11515, https://doi.org/10.1038/ncomms11515 (acccessed 2023-06-07T05:34:23).

[25] Y. Su, C. Burger, B.S. Hsiao, B. Chu, Characterization of TEMPO-oxidized cellulose nanofibers in aqueous suspension by small-angle X-ray scattering, *J. Appl. Cryst.* 47 (2) (2014) 788–798, https://doi.org/10.1107/s1600576714005020 (acccessed 2023-07-12T10:37:00).

[26] Pignon, F.; Challamel, M.; De Geyer, A.; Elchamaa, M.; Semeraro, E. F.; Hengl, N.; Jean, B.; Putaux, J. L.; Gicquel, E.; Bras, J.; et al. Breakdown and buildup mechanisms of cellulose nanocrystal suspensions under shear and upon relaxation probed by SAXS and SALS. *Carbohyd Polym* **2021**, *260*. DOI: ARTN 117751. 10.1016/j.carbpol.2021.117751.

[27] M. Uhlig, A. Fall, S. Wellert, M. Lehmann, S. Prévost, L. Wågberg, R. Von Klitzing, G. Nyström, Two-Dimensional Aggregation and Semidilute Ordering in Cellulose Nanocrystals, *Langmuir* 32 (2) (2016) 442–450, https://doi.org/10.1021/acs.langmuir.5b04008 (acccessed 2023-09-10T00:42:47).

[28] Y. Boluk, C. Danumah, Analysis of cellulose nanocrystal rod lengths by dynamic light scattering and electron microscopy, *J. Nanopart. Res.* 16 (1) (2014), https://doi.org/10.1007/s11051-013-2174-4 acccessed 2023-09-10T00:57:21.

[29] J. Van Rie, C. Schütz, A. Gençer, S. Lombardo, U. Gasser, S. Kumar, G. Salazar-Alvarez, K. Kang, W. Thielemans, Anisotropic Diffusion and Phase Behavior of Cellulose Nanocrystal Suspensions, *Langmuir* 35 (6) (2019) 2289–2302, https://doi.org/10.1021/acs.langmuir.8b03792 (acccessed 2023-06-13T05:30:57).

[30] L. Cristofolini, Synchrotron X-ray techniques for the investigation of structures and dynamics in interfacial systems, *Curr Opin Colloid in* 19 (3) (2014) 228–241, https://doi.org/10.1016/j.cocis.2014.03.006.

[31] O. Bikondoa, D. Carbone, X-Ray Photon Correlation Spectroscopy with Coherent Nanobeams: A Numerical Study, *Crystals* 10 (9) (2020) 766, https://doi.org/10.3390/cryst10090766 (acccessed 2023-06-09T20:15:15).

[32] F. Zhang, A.J. Allen, L.E. Levine, J. Ilavsky, G.G. Long, Ultra-Small-Angle X-ray Scattering-X-ray Photon Correlation Spectroscopy: A New Measurement Technique for In-Situ Studies of Equilibrium and Nonequilibrium Dynamics, *Metall Mater Trans A* 43a (5) (2012) 1445–1453, https://doi.org/10.1007/s11661-011-0790-0.

[33] Rosén, T.; Wang, R.; Zhan, C.; He, H.; Chodankar, S.; Hsiao, B. S. Cellulose nanofibrils and nanocrystals in confined flow: Single-particle dynamics to collective alignment revealed through scanning small-angle x-ray scattering and numerical simulations. *Physical Review E* **2020**, *101* (3). DOI: 10.1103/physreve.101.032610 (acccessed 2023-06-06T02:10:03).

[34] R. Wang, T. Rosen, C. Zhan, S. Chodankar, J. Chen, P.R. Sharma, S.K. Sharma, T. Liu, B.S. Hsiao, Morphology and Flow Behavior of Cellulose Nanofibers Dispersed in Glycols, *Macromolecules* 52 (15) (2019) 5499–5509, https://doi.org/10.1021/acs.macromol.9b01036 (acccessed 2023-06-11T17:24:19).

[35] A. Dorris, D.G. Gray, Gelation of cellulose nanocrystal suspensions in glycerol, *Cellul.* 19 (3) (2012) 687–694, https://doi.org/10.1007/s10570-012-9679-3 (acccessed 2023-06-12T19:01:19).

[36] T. Rosén, H. He, R. Wang, K. Gordeyeva, A.R. Motezakker, A. Fluerasu, L. D. Söderberg, B.S. Hsiao, Exploring nanofibrous networks with x-ray photon correlation spectroscopy through a digital twin, *Phys. Rev. E* 108 (1) (2023) 014607, https://doi.org/10.1103/physreve.108.014607 (acccessed 2023-09-10T06:01:10).

[37] H.J. Limbach, A. Arnold, B.A. Mann, C. Holm, ESPResSo - an extensible simulation package for research on soft matter systems, *Comput Phys Commun* 174 (9) (2006) 704–727, https://doi.org/10.1016/j.cpc.2005.10.005.

[38] J.D. Weeks, D. Chandler, H.C. Andersen, Role of Repulsive Forces in Determining the Equilibrium Structure of Simple Liquids, *J. Chem. Phys.* 54 (12) (1971) 5237–5247, https://doi.org/10.1063/1.1674820 (acccessed 2023-11-26T23:50:41).

[39] W. Chen, D.G. Gray, Interfacial Tension between Isotropic and Anisotropic Phases of a Suspension of Rodlike Particles, *Langmuir* 18 (3) (2002) 633–637, https://doi.org/10.1021/la001640i (acccessed 2023-09-05T03:10:21).

[40] D. Attia, N. Cohen, G. Ochbaum, Y. Levi-Kalisman, R. Bitton, R. Yerushalmi-Rozen, Nano-to-meso structure of cellulose nanocrystal phases in ethylene–glycol–water mixtures, *Soft Matter* 16 (36) (2020) 8444–8452, https://doi.org/10.1039/d0sm01025a (acccessed 2023-06-02T03:22:18).

[41] A. Pal, T. Zinn, M.A. Kamal, T. Narayanan, P. Schurtenberger, Anomalous Dynamics of Magnetic Anisotropic Colloids Studied by XPCS, *Small* 14 (46) (2018) 1802233, https://doi.org/10.1002/smll.201802233 (acccessed 2023-06-07T19:38:07).

[42] M.A. Kamal, A.V. Petukhov, A. Pal, Path-Dependent Self-Assembly of Magnetic Anisotropic Colloidal Peanuts, *J. Phys. Chem. B* 124 (27) (2020) 5754–5760, https://doi.org/10.1021/acs.jpcb.0c03771 (acccessed 2023-06-13T03:18:01).

[43] Pal, A.; Kamal, M. A.; Holmqvist, P.; Schurtenberger, P. Structure and dynamics of dense colloidal ellipsoids at the nearest-neighbor length scale. *Physical Review Research* **2021**, *3* (2). DOI: 10.1103/physrevresearch.3.023254 (acccessed 2023-06-13T03:20:16).

[44] T. Hoshino, M. Nakayama, S. Fujinami, T. Nakatani, Y. Kohmura, T. Kato, Static structure and dynamical behavior of colloidal liquid crystals consisting of hydroxyapatite-based nanorod hybrids, *Soft Matter* 15 (16) (2019) 3315–3322, https://doi.org/10.1039/c9sm00101h (acccessed 2023-06-14T02:50:18).

[45] S.W. Provencher, Contin - a General-Purpose Constrained Regularization Program for Inverting Noisy Linear Algebraic and Integral-Equations, *Comput Phys Commun* 27 (3) (1982) 229–242, https://doi.org/10.1016/0010-4655(82)90174-6.

[46] Johnston, D. C. Stretched exponential relaxation arising from a continuous sum of exponential decays (vol 74, art no 184430, 2006). *Phys Rev B* **2008**, *77* (17). DOI: ARTN 179901. 10.1103/PhysRevB.77.179901.

[47] Wang, R. F.; He, H. R.; Tian, J. J.; Chodankar, S.; Hsiao, B. S.; Rosén, T. Solvent-Dependent Dynamics of Cellulose Nanocrystals in Process-Relevant Flow Fields. *Langmuir* **2024**, *40* (25), 13319-13329. DOI: 10.1021/acs.langmuir.4c01846.

[48] M. Reiser, J.R Hallmann, J. Möller, K. Kazarian, D. Orsi, L. Randolph, H. Rahmann, F. Westermeier, E. Stellamanns, M. Sprung, Photo-controlled dynamics and transport in entangled wormlike micellar nanocomposites studied by XPCS, *Macromolecules* 55 (19) (2022) 8757–8765.

[49] A. Celzard, V. Fierro, R. Kerekes, Flocculation of cellulose fibres: new comparison of crowding factor with percolation and effective-medium theories, *Cellul.* 16 (6) (2009) 983–987, https://doi.org/10.1007/s10570-009-9314-0 (acccessed 2023-10-09T22:10:46).

[50] Roseker, W.; Hruszkewycz, S. O.; Lehmkühler, F.; Walther, M.; Schulte-Schrepping, H.; Lee, S.; Osaka, T.; Strüder, L.; Hartmann, R.; Sikorski, M.; et al. Towards ultrafast dynamics with split-pulse X-ray photon correlation spectroscopy at free electron laser sources. *Nature Communications* **2018**, *9*. DOI: ARTN 1704. 10.1038/s41467-018-04178-9.

[51] G. Grübel, G.B. Stephenson, C. Gutt, H. Sinn, T. Tschentscher, XPCS at the European X-ray free electron laser facility, *Nucl Instrum Meth B* 262 (2) (2007) 357–367, https://doi.org/10.1016/j.nimb.2007.05.015.

[52] B.W.J. McNeil, N.R. Thompson, X-ray free-electron lasers, *Nat Photonics* 4 (12) (2010) 814–821, https://doi.org/10.1038/nphoton.2010.239.

[53] S. Shafiei-Sabet, W.Y. Hamad, S.G. Hatzikiriakos, Rheology of Nanocrystalline Cellulose Aqueous Suspensions, *Langmuir* 28 (49) (2012) 17124–17133, https://doi.org/10.1021/la303380v (acccessed 2023-06-12T07:11:19).